GDCh

Research Articles

Angewandte
Chemie
International Edition
www.angewandte.org

Coordination Polymers **Hot Paper**

Linker Redox Mediated Control of Morphology and Properties in Semiconducting Iron-Semiquinoid Coordination Polymers**

Lei Wang, Robert J. Papoular, Noah E. Horwitz, Jiaze Xie, Arup Sarkar, Dario Campisi, Norman Zhao, Baorui Cheng, Garrett L. Grocke, Tengzhou Ma, Alexander S. Filatov, Laura Gagliardi, and John S. Anderson*

Abstract: The emergence of conductive 2D and less commonly 3D coordination polymers (CPs) and metal–organic frameworks (MOFs) promises novel applications in many fields. However, the synthetic parameters for these electronically complex materials are not thoroughly understood. Here we report a new 3D semiconducting CP $Fe_5(C_6O_6)_3$, which is a fusion of 2D Fe-semiquinoid materials and 3D cubic $Fe_x(C_6O_6)_y$ materials, by using a different initial redox-state of the C_6O_6 linker. The material displays high electrical conductivity (0.02 S cm^{-1}), broad electronic transitions, promising thermoelectric behavior ($S^2\sigma = 7.0 \times 10^{-9}$ W m^{-1} K^{-2}), and strong antiferromagnetic interactions at room temperature. This material illustrates how controlling the oxidation states of redox-active components in conducting CPs/MOFs can be a "pre-synthetic" strategy to carefully tune material topologies and properties in contrast to more commonly encountered post-synthetic modifications.

[*] Dr. L. Wang, Dr. N. E. Horwitz, J. Xie, Dr. A. Sarkar, Dr. D. Campisi, N. Zhao, B. Cheng, Dr. A. S. Filatov, Prof. Dr. J. S. Anderson
Department of Chemistry, University of Chicago
5735 S Ellis Ave, Chicago, IL 60637 (USA)
E-mail: jsanderson@uchicago.edu

Dr. R. J. Papoular
IRAMIS, Leon Brillouin Laboratory, CEA-Saclay
91191 Gif-sur-Yvette (France)

G. L. Grocke, T. Ma
Pritzker School of Molecular Engineering, University of Chicago
5735 S Ellis Ave, Chicago, IL 60637 (USA)

Prof. Dr. L. Gagliardi
Department of Chemistry, Pritzker School of Molecular Engineering, James Franck Institute and Chicago Center for Theoretical Chemistry, University of Chicago
5735 S Ellis Ave, Chicago, IL 60637 (USA)

[**]A previous version of this manuscript has been deposited on a preprint server (https://doi.org/10.26434/chemrxiv-2021-1v37x-v2).

Introduction

Introducing novel bulk electronic properties such as charge mobility or electrical conductivity into coordination polymers (CPs) and metal–organic frameworks (MOFs) has been an area of very active research in recent years.[1] These features, while interesting in their own right, are even more appealing when combined with the tunable topologies and structures that are hallmarks of CPs and MOFs.[2] Thus, this emerging class of materials has found many novel applications in chemical sensing,[3] electrochemical energy storage,[4] optoelectronics,[5] thermoelectrics,[6] magnetism and spintronics.[7] While the exploration of promising functionalities and applications in these materials has been a major focus, for instance in using sophisticated physical characterization methods[8] and theoretical calculations[9] to study carrier transport mechanisms, the exploration of their synthetic space[8d,10] is still nascent. This is particularly true when contrasted to the rich morphological, structural, defect, and phase space of more traditional MOF candidates which can largely be controlled by choice of synthetic conditions, additives, or linker morphology.[11]

When considering electronically complex CPs and MOFs, the redox-states of the metal and linker components are a critical factor.[12] For example, Sun et al. measured the electrical conductivity and activation energy for twenty different MOFs in four distinct structural families. They found that Fe-based MOFs displayed significantly higher conductivities and smaller charge activation energies due to in situ oxidation to form Fe$^{II/III}$ mixed valency in contrast to the other metals which maintain divalent oxidation states.[13] Similar examples can be seen for linkers. Quinone-based linkers are prototypical redox-active motifs and numerous examples of new conducting or magnetic CPs/MOFs have been reported using linkers of the form $(C_6O_4X_2)$ (X=H, F, Cl, Br, I, NO$_2$, CN).[14] Despite the importance of the final linker redox-state for materials structure and properties, leveraging different linker-redox states as a synthetic strategy, such as using different quinone redox-isomers in syntheses, has not been thoroughly investigated.

Taken to the limit of monocyclic quinones, hexahydroxybenzene (HHB) or tetrahydroxy-1,4-quinone (THQ), has the most accessible redox-isomers and several possible radical based intermediates (Figure 1).[10e,15] As such, this linker is an attractive target for incorporation into new materials, but also offers challenges in predicting or
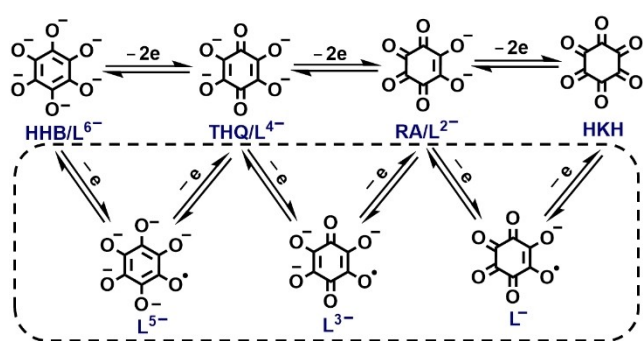
Figure 1. Multiple accessible oxidation states (top) and possible intermediates (in dashed box) of C_6O_6.

controlling the redox-state of resulting MOFs. The first 2D semiconducting MOF featuring this motif, Cu-HHB [Cu_3-$(C_6O_6)_2$], was synthesized in 2018 by reacting Cu^{II} with either HHB or THQ.[10e] This material displays good performance in lithium-ion battery and photoconductivity applications as illustrated by later reports,[4e,8c] but an interesting observation is that the same structure is formed regardless of the linker precursor oxidation state. Switching from Cu^{II} to a

more easily oxidized Fe^{II} ion results in two novel 3D conducting MOFs, namely **$Fe_{12}(C_6O_6)_6$** and **$Fe_8(C_6O_6)_6$**.[16] While similar, the connections between metals and linkers as well as the final oxidation states of the linkers in these two cubic structures are different (Figure 2A top), likely due to the subtle differences in reaction conditions. These examples provide concrete illustrations of how different materials can result from common or closely related precursors due to different synthetic protocols. This is particularly true in metal-semiquinoid based materials as spontaneous redox chemistry likely plays an important role upon material formation.

We were intrigued by the multiple accessible precursor redox-states of the C_6O_6 linkers in this family of materials, particularly in the context of varying material structure and properties. Herein, we present the synthesis of a new 3D semiconducting CP, **$Fe_5(C_6O_6)_3$**, which is generated by reacting Fe^{II} with the most reduced linker precursor HHB instead of THQ. In contrast to the Cu and Fe systems mentioned above, the use of a different redox-state of the linker results in a dramatically different structure. **Fe_5-$(C_6O_6)_3$** consists of hexagonal layers with a staggered AB stacking. Moreover, these layers are further bridged by axial Fe centers through Fe–O bonds to generate a 3D material
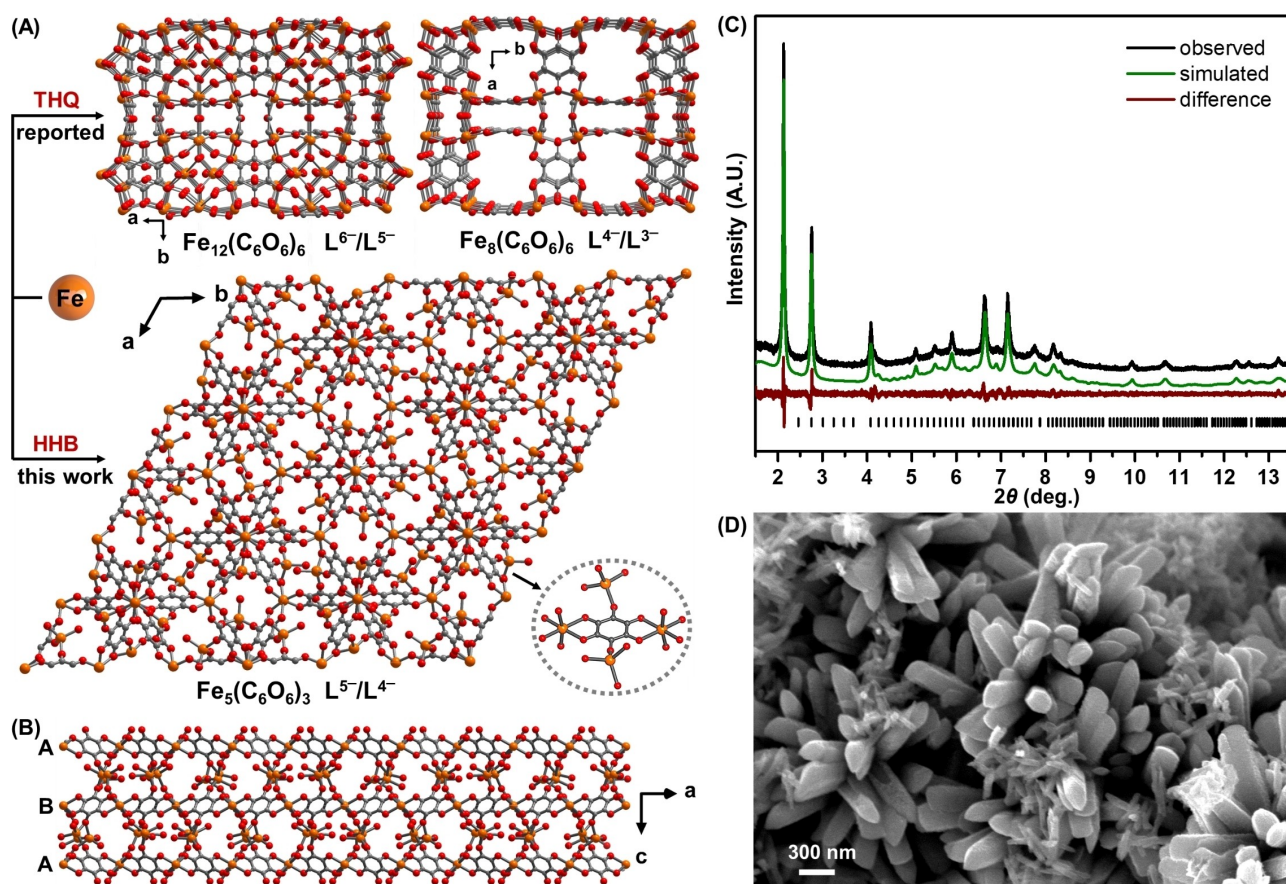

Figure 2. A) Schematic illustration of the previously reported 3D materials **$Fe_{12}(C_6O_6)_6$**, **$Fe_8(C_6O_6)_6$** and the **$Fe_5(C_6O_6)_3$** material reported here. B) Orientation of neighboring layers in **$Fe_5(C_6O_6)_3$**. Orange: Fe, red: O, grey: C; coordinated solvent molecules are omitted for clarity. C) Comparison of the synchrotron X-ray powder diffraction data (295 K, $\lambda = 0.458093$ Å) and calculated (Le Bail) pattern in $P6_3$. D) SEM image of **$Fe_5(C_6O_6)_3$** powder.

(Figure 2A bottom). This novel topology is reminiscent of retrofitting modifications used in carboxylate-based MOFs to affect material properties,[17] as well as proposed approaches to promote delocalization of charge by extending into three dimensions.[9d] The optical absorption, conductivity, Seebeck coefficient, and magnetic susceptibility of **Fe₅(C₆O₆)₃** have been explored, revealing redox-state and structurally dependent trends. Our studies demonstrate that, in contrast to post-synthetic modifications, pre-synthetically controlling the redox-states of components in conductive or magnetic coordination polymers is an important parameter for encoding properties and functionalities.

Results and Discussion

Synthesis and structure

Fe₅(C₆O₆)₃ was prepared by reacting anhydrous $FeCl_2$ with HHB in dimethylformamide (DMF) at 100 °C for three days under an inert atmosphere. These synthetic conditions are similar to those reported for **Fe₁₂(C₆O₆)₆** and **Fe₈(C₆O₆)₆** but with slight modifications. Control experiments by varying the linker precursor (HHB or THQ) in these reaction conditions indicate that the initial oxidation states of the organic linkers can affect the reaction kinetics and thermodynamics, likely due to spontaneous redox chemistry during the material synthesis (Figure S2). Analysis of the headspace of the reaction vessel by gas chromatography shows the presence of H_2, confirming this proposed redox chemistry (Figure S1). Thus, the oxidation state of the organic linkers is an important factor in the synthesis of conductive CPs/MOFs in addition to the choice of metal salt, solvent, and temperature that are more commonly considered in conventional MOF syntheses. X-ray powder diffraction (PXRD) data suggests **Fe₅(C₆O₆)₃** is a polycrystalline material (Figure S3–S4), and the pattern can be indexed in a primitive hexagonal unit cell $a = b = 24.63$ Å, $c = 14.93$ Å, $\alpha = \beta = 90°$, and $\gamma = 120°$ (Figure S5). The Le Bail fit shows that essentially all of the observed Bragg peaks can be accounted for by this unit cell and the $P6_3$ space group (Figure 2C, Figure S5–S8). Scanning electron microscopy (SEM) images show a hexagonal rod- or needle-like morphology which is also consistent with the structural assignment (Figure 2D). The size of the particles ranges from 200 nm to 1 μm due to substantial interparticle growth.

The structure was solved by scripting the algebraic computations of the molecular fragments and the resulting framework layers with a python programming language that followed by simulated annealing global optimizations (see the Supporting Information for the detailed description of the structure solution process, variable models considered and programmed Python scripts). The final structure of **Fe₅(C₆O₆)₃**, as depicted in Figure 2A, shows that 40 % of the Fe atoms are octahedrally coordinated with C_6O_6 units to form extended hexagonal layers. These hexagonal layers are reminiscent of similar layers in quinone-based materials and are significantly different from the pseudo-cubic structures observed for the **Fe₁₂(C₆O₆)₆**/**Fe₈(C₆O₆)₆** materials previously

reported. However, in **Fe₅(C₆O₆)₃** the layers are packed in a staggered ABAB pattern and neighboring layers have a mirror-like orientation (Figure 2B). These 2D layers are further bridged by extra Fe atoms (60 %) and are extended into a 3D structure in a distinct manner from the layered lanthanide metal–organic frameworks or pillared Cu-THQ materials.[18] This results in two distinct coordination environments for Fe: octahedral intralayer and pseudotetrahedral interlayer (Figure 2A inset). We note that none of the O atoms in **Fe₅(C₆O₆)₃** bridge two Fe centers. This contrasts to the cubic materials **Fe₁₂(C₆O₆)₆** and **Fe₈(C₆O₆)₆** where some O atoms form μ_2 bridges to provide six-coordinate Fe centers. The coordination environment of the interlayer Fe atoms in **Fe₅(C₆O₆)₃** is completed by solvent molecules, however, the positions of these solvents are unsurprisingly highly disordered, thus precluding a precise determination of their positions. The Rietveld refinement of the model lacking exact positions for solvent molecules shows a satisfactory agreement with the experimental pattern (a final R_p value is 11.1 %, Table S4). Combustion and thermogravimetric analysis are consistent with this structural assignment with a formula of $Fe_5(C_6O_6)_3(H_2O)_3(C_3H_7NO)_3$ (Table S1 and Figure S14). Digestion experiment further confirms the existence of DMF in the material (Figure S15). Furthermore, N_2 uptake experiments suggest a type II isotherm and a measured BET surface area of 41.7 m^2g^{-1} (Figure S16). Both results indicate a lack of porosity of the material as expected from the staggered AB packing and the existence of interlayer bridging Fe with coordinated solvent molecules.

Oxidation states of the components

X-ray photoelectron spectroscopy (XPS) was initially used to probe the oxidation state of the Fe ions in **Fe₅(C₆O₆)₃** (Figure S17). A broad Fe $2p_{3/2}$ peak is observed which is centered around 710.5 eV. The position of this peak suggests a mixed valent material as compared with values in iron oxides (FeO ≈ 709.5 eV, Fe_2O_3 ≈ 711 eV).[19] Further corroboration of mixed valency is obtained from ^{57}Fe Mössbauer spectroscopy where three sets of signals are observed in the spectrum (Figure 3A and Figure S18). One of the Fe sites (≈ 24 %) has an isomer shift (δ) of 0.665(1) mm/s^{-1} and a quadrupole splitting (ΔE_Q) of 0.933(7) mm s^{-1} while another (≈ 49 %) has a δ of 0.683(2) mm s^{-1} and a ΔE_Q of 1.308(14) mm s^{-1}. Both of these sets of parameters are consistent with an assignment of high-spin Fe^{III} centers although the observed δ's are slightly larger than those assigned to high spin Fe^{III} centers in iron-semiquinone complexes and CPs.[14b,c,20] For instance, the δ is 0.574-(2) mm s^{-1} for the 3D $(NBu_4)_2[Fe_2(dhbq)_3]$ material.[14b] The larger isomer shift may be due to a decrease in electron density on the Fe^{III} centers in our material.[14c] The third feature (≈ 27 %) has a δ of 1.269(3) mm s^{-1} and a ΔE_Q of 3.105(4) mm s^{-1} which distinctly assigns this site as a high-spin Fe^{II} species.[21] Given the overall oxidation states of the Fe centers obtained from Mössbauer spectroscopy and the molecular formula, the oxidation state of the organic linkers
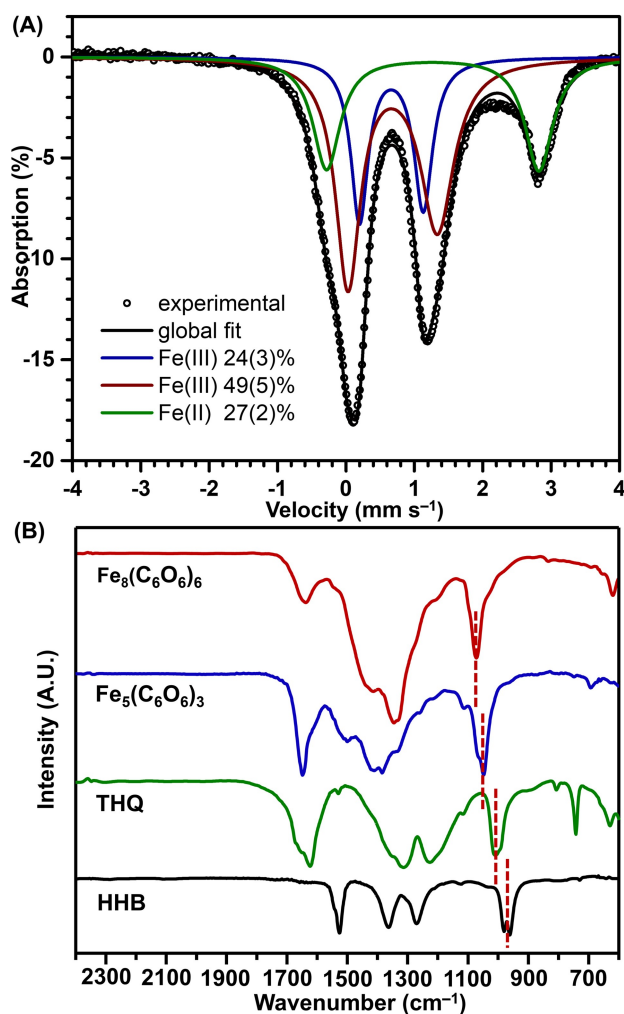
Figure 3. A) ^{57}Fe Mössbauer spectrum recorded at 77 K and fitting results for three species. B) FT-IR spectrum of the HHB, THQ, **Fe$_5$(C$_6$O$_6$)$_3$** and **Fe$_8$(C$_6$O$_6$)$_6$** recorded in transmission mode (dashed red lines mark the C–O stretching bands).

is estimated to be −4.5 per C$_6$O$_6$ unit. These results suggest both the metal centers and organic linkers are spontaneously oxidized during the material formation, as suggested from the detection of H$_2$ in the reactions (see above, Figure S1).

Corroborating evidence of the oxidation state of the linkers was obtained from Fourier-transform infrared (FT-IR) spectroscopy. As shown in Figure 3B, after coordination a stretching band around 1000 cm^{-1} in **Fe$_5$(C$_6$O$_6$)$_3$**, tentatively assigned to a C–O vibration (see Figure S19 for explanation), shifts to a higher frequency compared to the free ligand HHB. This shift suggests a more oxidized linker in **Fe$_5$(C$_6$O$_6$)$_3$** than in the starting ligand, as a shift to a lower frequency would be normally expected after coordination for redox-inactive linkers. A similar shift is also observed between THQ and **Fe$_8$(C$_6$O$_6$)$_6$** where the linker is also reported to be oxidized. In addition, comparison of the two Fe materials reveals a slightly lower C–O stretching frequency in **Fe$_5$(C$_6$O$_6$)$_3$** than in **Fe$_8$(C$_6$O$_6$)$_6$**. This supports a more reduced linker oxidation state in the former material, as would be consistent with the formal oxidation state of

roughly −4.5 which would arise from mixed valency between L^{5-}/L^{4-} for the HHB linkers as indicated by Mössbauer analysis. In comparison, the calculated average charge from Mössbauer analysis is −5.4 and −3.6 per C$_6$O$_6$ unit in the related cubic materials **Fe$_{12}$(C$_6$O$_6$)$_6$** and **Fe$_8$(C$_6$O$_6$)$_6$**, potentially suggesting a mixed valency of L^{6-}/L^{5-} and L^{4-}/L^{3-} respectively. The significantly different formal linker oxidation states in these materials, in addition to their distinct structures, illustrates the rich composition space that is available for these conductive CPs/MOFs.

Electronic properties

The electronic properties of **Fe$_5$(C$_6$O$_6$)$_3$** were then explored with a variety of techniques. UV-vis-NIR diffuse reflectance spectroscopy shows four major absorption signals (Figure 4A, S20). The sharp peak centered at around 300 nm, which is also seen in the free ligand, is assigned to a $\pi \rightarrow \pi^*$ transition in the organic linkers.[22] The shoulder-like peak at around 370 nm, which is more obvious in the solution spectra of a suspension (Figure S20), is tentatively assigned to an internal transition from the radical linkers (L^{5-}) although this transition occurs at around 470 nm in the chloranilate based radical (CA^{3-}) and the 2,5-dihydroxy-1,4-benzoquinone based radical (DHBQ^{3-}).[23] The peak at around 560 nm in **Fe$_5$(C$_6$O$_6$)$_3$** is reasonably assigned as a ligand-to-metal charge transfer band, which is similarly observed in a semiquinone-catecholate based mononuclear iron complex and iron semiquinoid-based MOFs.[4f, 22] Most notably, **Fe$_5$(C$_6$O$_6$)$_3$** displays a strong and broad absorption starting from 650 nm and tailing to 2700 nm. This broad absorption is indicative of an intervalence charge transfer (IVCT) and can be classified as Class II/III according to the Robin–Day formalism.[12b] It is worthwhile to note that the first observation of Class II/III ligand-based mixed-valency in a MOF was in (NBu$_4$)$_2$Fe$_2$(dhbq)$_3$ with an IVCT transition band centered at around 1428 nm ($\nu_{max} = 7000$ cm^{-1}).[14b] Later, several metal–semiquinoid frameworks have displayed Robin–Day Class II/III mixed-valency with broad absorbances in the mid-IR region extending to the near-IR region.[14e] Even among this group, our material features a notably broad adsorption ranging from the visible to mid-IR region. The breadth of this feature may be attributed to dual mixed valency from both metal centers and organic linkers. An estimated band gap (E_g) of 0.75 eV is obtained from a Tauc plot with a direct band gap fitting (Figure 4A inset) and is very similar to that observed in the two 3D **Fe$_{12}$(C$_6$O$_6$)$_6$/Fe$_8$(C$_6$O$_6$)$_6$** materials supporting that all of these compounds feature mixed-valency.

The electrical conductivity (σ) of **Fe$_5$(C$_6$O$_6$)$_3$** was measured as an average of $2.0(4) \times 10^{-2}$ S cm^{-1} on pressed pellets at room temperature using a two-probe method (Figure S21a). Although this two-probe method likely underestimates the intrinsic conductivity of this material, this conductivity is slightly higher than **Fe$_8$(C$_6$O$_6$)$_6$** and **Fe$_{12}$-(C$_6$O$_6$)$_6$** despite the more anisotropic layered structure in **Fe$_5$(C$_6$O$_6$)$_3$**.[1d, 2d] Variable-temperature conductivity measurements over 140–295 K show that the conductance of the

Angew. Chem. Int. Ed. **2022**, *61*, e202207834 (4 of 9)

© 2022 The Authors. Angewandte Chemie International Edition published by Wiley-VCH GmbH
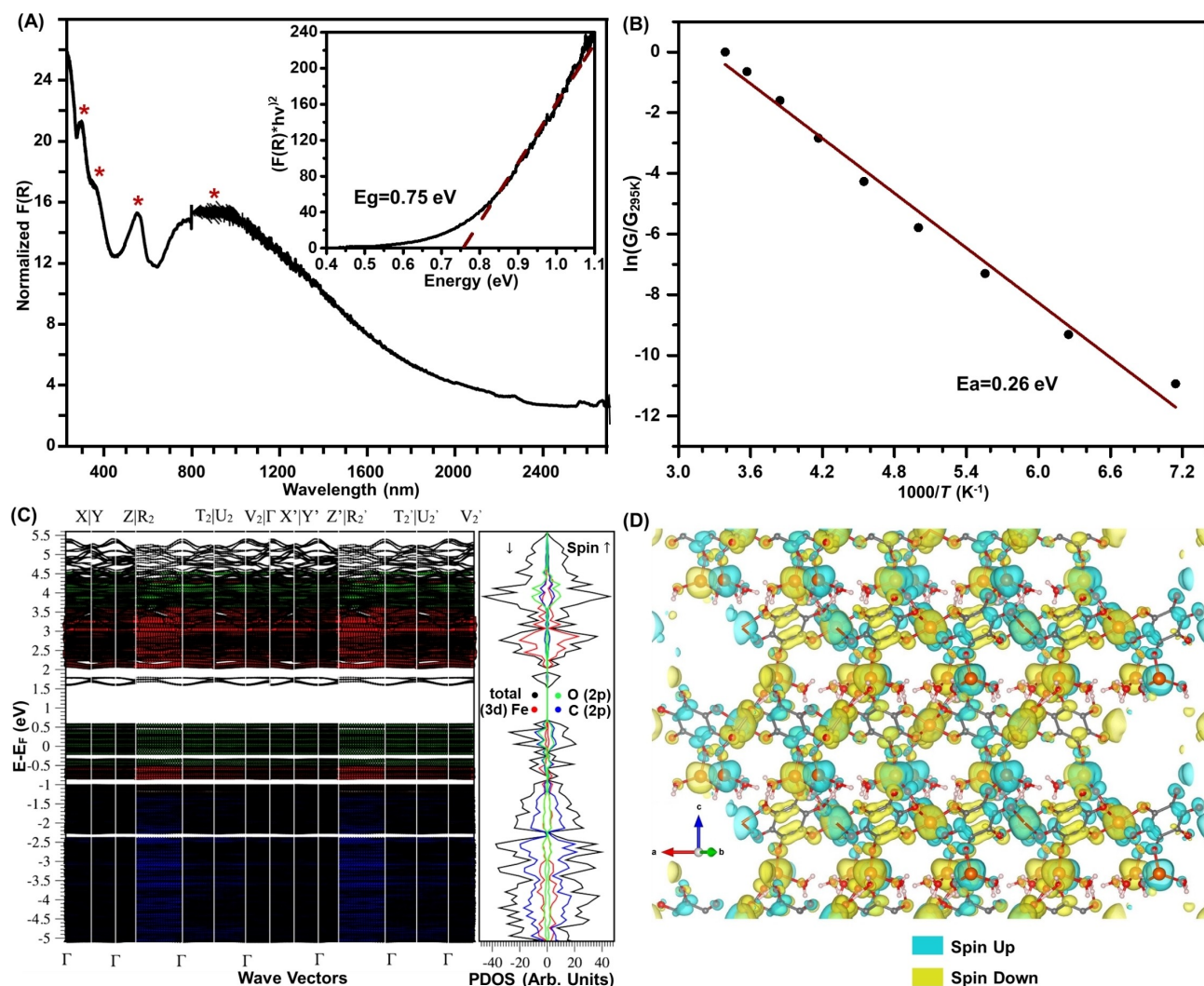
Figure 4. A) UV-vis-NIR diffuse reflectance spectrum (four absorption features are marked; inflection around 800 nm is due to lamp change, F(R) is the Kubelka-Munk conversion of the raw diffuse reflectance). Inset is the Tauc plot with a direct band gap fitting (dashed line) for the near-IR feature. B) Arrhenius fitting (red line) of the variable-temperature conductance (G) data (black dots) by the equation of $G = G_0 \exp(E_a/kT)$. C) Computed PBE-D3(BJ) + U Hubbard corrected total and projected density-of-states (pDOS) and bands (pBANDS) using a reduced cell. D) Spin density isosurface plot (isovalue 0.004 e Å^{-3}) of the anti-ferromagnetic ground state.

material increases with temperature, indicative of bulk semiconducting behavior (Figure S21b). Arrhenius fitting to the nearest-neighbours hopping (NNH) model[14e,24] suggests a small activation energy (E_a) of 0.26 eV (Figure 4B). This value is similar to that reported for the **Fe$_8$(C$_6$O$_6$)$_6$** and **Fe$_{12}$(C$_6$O$_6$)$_6$**, which again can be ascribed to dual mixed-valency that facilitates redox hopping between neighboring ligands or metal centers.[16]

Calculations using the PBE-D3(BJ)[25] exchange-correlation functional with dispersion correction[26] as implemented in the VASP code[27] were then performed to study **Fe$_5$-(C$_6$O$_6$)$_3$** (see Supporting Information for details). This functional is widely employed to predict MOF structures and properties.[16b,28] The calculations were performed for the singlet spin state, which is the anti-ferromagnetic ground state according to magnetic susceptibility measurements (see below). The model was optimized using a reduced cell ($P6_3$,

$a = 14.262$ Å, $c = 14.998$ Å, 118 atoms) through symmetry transformation. Estimated bond lengths along with the experimental values are reported in Table S3. Table S3 reports the average values of the Fe–O and C–O bond lengths, which result in good agreement with the experiments and another well-studied DFT functional.

In order to get insight into the electronic structure and band properties of **Fe$_5$(C$_6$O$_6$)$_3$**, we corrected the strong on-site Coulomb interaction of localized d orbitals by performing single point calculations at the PBE-D3(BJ) optimized geometry with the Hubbard correction (DFT + U method)[29] and special K-points grid for band structures. The spin density isosurface (Figure 4D) shows that out of ten Fe-centers in the unit cell, five Fe centers possess large populations of spin up and the remaining five Fe centers show large spin down populations, which proved that the chosen anti-ferromagnetic configuration did not change

during geometry optimization. Benzene rings of $Fe_5(C_6O_6)_3$ present a large population of spin down and up in which the radicals are mainly localized on the oxygen atoms that bind to the Fe-center.

The Hubbard U value is set to 4 eV for the Fe centers. The selected U value well reproduces the band gap of Fe-based MOF (0.73 eV) and is consistent with the U value computed for analogous systems.[16b,30] The projected density of states (PDOS shown in Figure 4C) is characterized by large dominating bands in an energy window between −5 eV and 0.6 eV with respect to the Fermi level, set at 0 eV, for the valence band and a series of conductive bands in an energy window between 1.5 eV and 5.5 eV. Moreover a mid band state occurs between 1.6 eV and 1.9 eV. The system has semiconductor character and the presence of mid-gap states confirms a radical character of the Fe-MOF, as also found in different graphene-like structures using the tight-binding model.[31] The valence band is dominated by C and O 2p electrons, whereas the conductive band is dominated by Fe 3d electrons. This trend is confirmed by the projected band structures (shown in Figure 4C) in which maxima at gamma point are characterized by a series of bands with π-d symmetry.

Thermoelectric properties

The thermoelectric properties of $Fe_5(C_6O_6)_3$ were also explored and the Seebeck coefficient (*S*) was measured as $+59.3\ \mu V\,K^{-1}$ at room temperature, suggesting a p-type thermoelectric behavior (Figure S23c).[6] Interestingly, $Fe_8(C_6O_6)_6$ exhibits n-type thermoelectric behavior ($-194.0\ \mu V\,K^{-1}$) with a lower conductivity ($3.9(3) \times 10^{-3}\ S\,cm^{-1}$) at room temperature (Figure S22b, S23d). Moreover, $Fe_{12}(C_6O_6)_6$ was also previously reported with an n-type thermoelectric behavior ($-130\ \mu V\,K^{-1}$) and an even lower conductivity ($2.7 \times 10^{-4}\ S\,cm^{-1}$) at room temperature. The calculated power factor ($S^2\sigma$) is $4.6 \times 10^{-10}\ W\,m^{-1}\,K^{-2}$ for $Fe_{12}(C_6O_6)_6$, $7.0 \times 10^{-9}\ W\,m^{-1}\,K^{-2}$ for $Fe_5(C_6O_6)_3$ and $1.5 \times 10^{-8}\ W\,m^{-1}\,K^{-2}$ for $Fe_8(C_6O_6)_6$ respectively, following a similar increasing trend as the oxidation states of the linkers in this series of materials (Figure S24). This trend potentially demonstrates that the linker redox states can be a useful "pre-synthetic" tool to optimize the thermoelectric conversion in conducting CPs/MOFs. Still, these values are lower than those reported for other 2D conductive MOFs. For instance, a high $S^2\sigma$ value of $8.3 \times 10^{-7}\ W\,m^{-1}\,K^{-2}$ has been reported for the hexaiminotriphenylene based MOF $Ni_3(HITP)_2$ and a record of $2.0 \times 10^{-6}\ W\,m^{-1}\,K^{-2}$ was reported for the perthiolated coronene based MOF Ni-PTC.[6b,d] The lower power factor of 3D materials is mostly ascribed to their lower electrical conductivity compared to the 2D conductive MOFs mentioned above, although both a high σ and *S* is desirable to achieve a high power factor. A critical disadvantage in these 3D materials is that redox hopping is the major contributor to conductivity while high metal-ligand covalency and strong in-plane π-d conjugation are more efficient for carrier transport in the 2D MOFs.[1d,2d,18] As the primary challenge for developing high performance

thermoelectric CPs/MOFs is improving charge carrier mobility, both "pre-synthetic" strategies (i.e. π-d conjugation enhancement) and post-synthetic modifications (i.e., doping) are promising approaches for further optimization.[6a,32]

Magnetic properties

$Fe_5(C_6O_6)_3$ also displays interesting magnetic properties. DC magnetic susceptibility measurements were performed and the experimental $\chi_M T$ per formula unit decreases almost linearly from 300 K to around 80 K (Figure 5A). This behavior suggests the existence of a dominant antiferromagnetic exchange coupling. Moreover, the observed $\chi_M T$ value at 300 K is $9.53\ cm^3\,K\,mol^{-1}$ for each $Fe_5(C_6O_6)_3$ unit. This value is much smaller than the estimated magnetically uncoupled spin-only value for the number of Fe and linker spin centers implied from Mössbauer analysis ($\chi_M T \approx 20\ cm^3\,K\,mol^{-1}$) which is also consistent with antiferromagnetic exchange.[16a] The presence of odd-electron linkers as well as mixed-valency between Fe centers suggests that superexchange, double exchange, and direct exchange pathways may all be present in $Fe_5(C_6O_6)_3$. While assigning the agency and importance of specific coupling pathways is
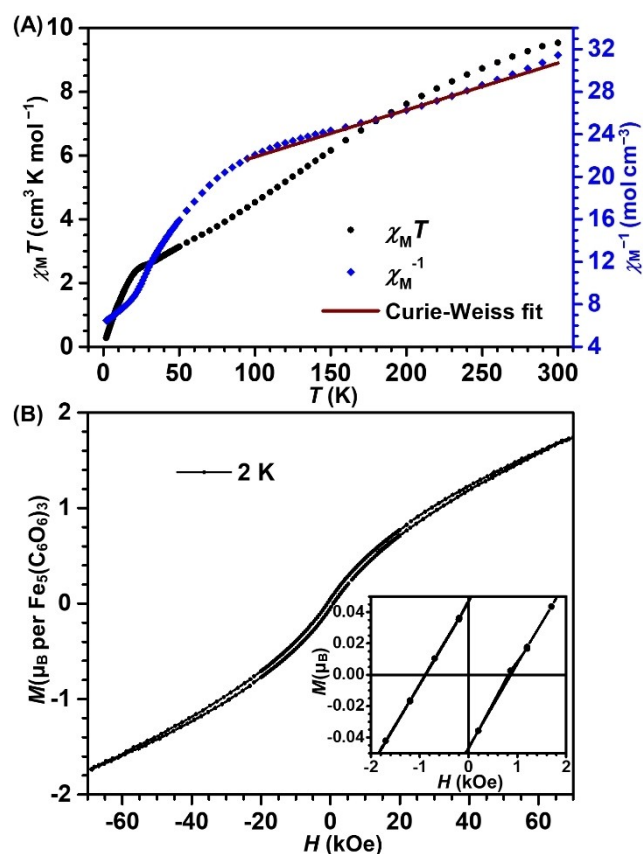

Figure 5. A) Plot of $\chi_M T$, χ_M^{-1} vs T from 300 K to 2 K and the linear Curie–Weiss fit in the high temperature region from the equation of $\chi_M = C/(T - \theta_{CW})$. C is the Curie constant and θ_{CW} is the Weiss constant. B) Variable-field magnetization data collected at 2 K. Inset shows the coercive field of 880 Oe.

challenging due to this complexity, fitting the χ_M^{-1} data with the Curie–Weiss law from 300 K to 80 K shows a large Weiss constant (θ_{CW}) of -400.7 K, supporting dominant antiferromagnetic character (Figure 5A). Interestingly, $\mathbf{Fe_{12}(C_6O_6)_6}$ also displays a decreasing $\chi_M T$ with decreasing temperature. The Curie–Weiss fit of $\mathbf{Fe_{12}(C_6O_6)_6}$ gives a Weiss constant of -219.37 K while the Co and Mn analogues have much smaller Weiss constants of -73.86 K and -47.95 K respectively.

In addition to the general antiferromagnetic trend in the susceptibility data, there is also a clear inflection at ≈ 30 K which displays some field dependence (Figure S25). Variable-temperature zero-field-cooled and field-cooled DC magnetization data (Figure S26) show a divergence at 30 K, likely suggesting some long-range interactions.[33] We have attempted to interrogate this behavior with variable-temperature AC susceptibility measurements, however only weak signals were observed. The data shows a broad cusp-like peak for the in-phase susceptibility (χ_M'), and a noticeable rising anomaly for the out-of-phase susceptibility (χ_M'') at around 10 K at low frequencies (Figure S27). While weak, these features may also be consistent with long-range magnetic interactions at low temperature.[33,34] Variable field magnetization data were also collected at 10 K, 5 K and 2 K, respectively. Each temperature indicates the presence of magnetic hysteresis, with corresponding coercive fields of $H_C = 148$ Oe, 415 Oe, and 880 Oe respectively (Figure 5B, S28).

The complicated geometric pattern, multiple possible exchange interactions in the system, and the small AC signals make interpreting the magnetic behavior of this material challenging. A potential explanation for the data is a coexistence of antiferromagnetic and spin-glass states at low temperature, which could arise from strong coupling within the 2D planes with a relatively weak antiferromagnetic exchange between the layers giving rise to spin-canting due to the mirrored interlayer orientation.[34,35] Indeed, strong intralayer and weak interlayer coupling in related hexagonal chloranilate frameworks have been observed and are dependent on the interlayer spacing.[14c,23b] Nevertheless, this proposal is speculative in our system and further studies, such as exchange of the interlayer metals with diamagnetic ions, will be required to thoroughly understand the magnetic behavior.

Conclusion

In summary, here we report a new 3D semiconducting material $\mathbf{Fe_5(C_6O_6)_3}$ generated from Fe^{II} and the most reduced version of HHB. This material is composed of AB stacked hexagonal planes further bridged by Fe–O bonds to generate a 3D structure that features intrinsic dual mixed valency. $\mathbf{Fe_5(C_6O_6)_3}$ is distinct from two previously reported $\mathbf{Fe_{12}(C_6O_6)_6}/\mathbf{Fe_8(C_6O_6)_6}$ materials in terms of topology, connectivity, and the final oxidation states of the linkers. It also displays relatively high electrical conductivity, broad absorptions across the visible and near-IR region, interesting thermoelectric behavior, and strong antiferromagnetic inter-

actions. Together these properties suggest that this material has promising applications in photo sensing, efficient thermoelectric conversion, and magnetic studies. These results highlight that redox-active components with multiple accessible oxidation states can be an important synthetic parameter in exploring the phase-space of conductive CPs/MOFs via "bottom-up" synthetic strategies. This approach illustrates an avenue which is orthogonal to post-synthetic modifications to enrich the library of multifunctional conductive inorganic-organic hybrid materials.

Conflict of Interest

The authors declare no conflict of interest.

Data Availability Statement

The data that support the findings of this study are available in the supplementary material of this article.

[1] a) D. M. D'Alessandro, J. R. R. Kanga, J. S. Caddy, *Aust. J. Chem.* **2011**, *64*, 718–722; b) C. H. Hendon, D. Tiana, A. Walsh, *Phys. Chem. Chem. Phys.* **2012**, *14*, 13120–13132; c) L. Sun, M. G. Campbell, M. Dincă, *Angew. Chem. Int. Ed.* **2016**, *55*, 3566–3579; *Angew. Chem.* **2016**, *128*, 3628–3642; d) L. S. Xie, G. Skorupskii, M. Dincă, *Chem. Rev.* **2020**, *120*, 8536–8580.

[2] a) M. Ko, L. Mendecki, K. A. Mirica, *Chem. Commun.* **2018**, *54*, 7873–7891; b) M. D. Allendorf, R. Dong, X. Feng, S. Kaskel, D. Matoga, V. Stavila, *Chem. Rev.* **2020**, *120*, 8581–8640; c) M. Wang, R. Dong, X. Feng, *Chem. Soc. Rev.* **2021**, *50*, 2764–2793; d) C. Li, L. Zhang, J. Chen, X. Li, J. Sun, J. Zhu, X. Wang, Y. Fu, *Nanoscale* **2021**, *13*, 485–509.

[3] a) I. Stassen, N. Burtch, A. Talin, P. Falcaro, M. Allendorf, R. Ameloot, *Chem. Soc. Rev.* **2017**, *46*, 3185–3241; b) M. G.

Campbell, D. Sheberla, S. F. Liu, T. M. Swager, M. Dincă, *Angew. Chem. Int. Ed.* **2015**, *54*, 4349–4352; *Angew. Chem.* **2015**, *127*, 4423–4426; c) J. Huang, Y. He, M.-S. Yao, J. He, G. Xu, M. Zeller, Z. Xu, *J. Mater. Chem. A* **2017**, *5*, 16139–16143.

[4] a) J. Liu, X. Song, T. Zhang, S. Liu, H. Wen, L. Chen, *Angew. Chem. Int. Ed.* **2021**, *60*, 5612–5624; *Angew. Chem.* **2021**, *133*, 5672–5684; b) D. Sheberla, J. C. Bachman, J. S. Elias, C.-J. Sun, Y. Shao-Horn, M. Dincă, *Nat. Mater.* **2017**, *16*, 220–224; c) D. Feng, T. Lei, M. R. Lukatskaya, J. Park, Z. Huang, M. Lee, L. Shaw, S. Chen, A. A. Yakovenko, A. Kulkarni, J. Xiao, K. Fredrickson, J. B. Tok, X. Zou, Y. Cui, Z. Bao, *Nat. Energy* **2018**, *3*, 30–36; d) K. W. Nam, S. S. Park, R. dos Reis, V. P. Dravid, H. Kim, C. A. Mirkin, J. F. Stoddart, *Nat. Commun.* **2019**, *10*, 4948; e) Q. Jiang, P. Xiong, J. Liu, Z. Xie, Q. Wang, X.-Q. Yang, E. Hu, Y. Cao, J. Sun, Y. Xu, L. Chen, *Angew. Chem. Int. Ed.* **2020**, *59*, 5273–5277; *Angew. Chem.* **2020**, *132*, 5311–5315; f) M. E. Ziebel, C. A. Gaggioli, A. B. Turkiewicz, W. Ryu, L. Gagliardi, J. R. Long, *J. Am. Chem. Soc.* **2020**, *142*, 2653–2664.

[5] a) V. Stavila, A. A. Talin, M. D. Allendorf, *Chem. Soc. Rev.* **2014**, *43*, 5994–6010; b) H. Liu, Y. Wang, Z. Qin, D. Liu, H. Xu, H. Dong, W. Hu, *J. Phys. Chem. Lett.* **2021**, *12*, 1612–1630; c) H. Arora, R. Dong, T. Venanzi, J. Zscharschuch, H. Schneider, M. Helm, X. Feng, E. Cánovas, A. Erbe, *Adv. Mater.* **2020**, *32*, 1907063.

[6] a) Y. Lu, D. J. Young, *Dalton Trans.* **2020**, *49*, 7644–7657; b) L. Sun, B. Liao, D. Sheberla, D. Kraemer, J. Zhou, E. A. Stach, D. Zakharov, V. Stavila, A. A. Talin, Y. Ge, M. D. Allendorf, G. Chen, F. Léonard, M. Dincă, *Joule* **2017**, *1*, 168–177; c) J. Park, A. C. Hinckley, Z. Huang, G. Chen, A. A. Yakovenko, X. Zou, Z. Bao, *J. Am. Chem. Soc.* **2020**, *142*, 20531–20535; d) Z. Chen, Y. Cui, Y. Jin, L. Liu, J. Yan, Y. Sun, Y. Zou, Y. Sun, W. Xu, D. Zhu, *J. Mater. Chem. C* **2020**, *8*, 8199–8205.

[7] a) A. E. Thorarinsdottir, T. D. Harris, *Chem. Rev.* **2020**, *120*, 8716–8789; b) X. Song, X. Wang, Y. Li, C. Zheng, B. Zhang, C.-a. Di, F. Li, C. Jin, W. Mi, L. Chen, W. Hu, *Angew. Chem. Int. Ed.* **2020**, *59*, 1118–1123; *Angew. Chem.* **2020**, *132*, 1134–1139; c) Y. Misumi, A. Yamaguchi, Z. Zhang, T. Matsushita, N. Wada, M. Tsuchiizu, K. Awaga, *J. Am. Chem. Soc.* **2020**, *142*, 16513–16517.

[8] a) R. Dong, P. Han, H. Arora, M. Ballabio, M. Karakus, Z. Zhang, C. Shekhar, P. Adler, P. S. Petkov, A. Erbe, S. C. B. Mannsfeld, C. Felser, T. Heine, M. Bonn, X. Feng, E. Cánovas, *Nat. Mater.* **2018**, *17*, 1027–1032; b) R. W. Day, D. K. Bediako, M. Rezaee, L. R. Parent, G. Skorupskii, M. Q. Arguilla, C. H. Hendon, I. Stassen, N. C. Gianneschi, P. Kim, M. Dincă, *ACS Cent. Sci.* **2019**, *5*, 1959–1964; c) J. Nyakuchena, S. Ostresh, D. Streater, B. Pattengale, J. Neu, C. Fiankor, W. Hu, E. D. Kinigstein, J. Zhang, X. Zhang, C. A. Schmuttenmaer, J. Huang, *J. Am. Chem. Soc.* **2020**, *142*, 21050–21058; d) J.-H. Dou, M. Q. Arguilla, Y. Luo, J. Li, W. Zhang, L. Sun, J. L. Mancuso, L. Yang, T. Chen, L. R. Parent, G. Skorupskii, N. J. Libretto, C. Sun, M. C. Yang, P. V. Dip, E. J. Brignole, J. T. Miller, J. Kong, C. H. Hendon, J. Sun, M. Dincă, *Nat. Mater.* **2021**, *20*, 222–228.

[9] a) S. Chen, J. Dai, X. C. Zeng, *Phys. Chem. Chem. Phys.* **2015**, *17*, 5954–5958; b) M. E. Foster, K. Sohlberg, C. D. Spataru, M. D. Allendorf, *J. Phys. Chem. C* **2016**, *120*, 15001–15008; c) E. Zojer, C. Winkler, *J. Phys. Chem. Lett.* **2021**, *12*, 7002–7009; d) K. N. Le, J. L. Mancuso, C. H. Hendon, *ACS Appl. Electron. Mater.* **2021**, *3*, 2017–2023; e) Z. Zhang, D. Dell'Angelo, M. R. Momeni, Y. Shi, F. A. Shakib, *ACS Appl. Mater. Interfaces* **2021**, *13*, 25270–25279.

[10] a) H. Maeda, R. Sakamoto, H. Nishihara, *Langmuir* **2016**, *32*, 2527–2538; b) M. Hmadeh, Z. Lu, Z. Liu, F. Gándara, H. Furukawa, S. Wan, V. Augustyn, R. Chang, L. Liao, F. Zhou, E. Perre, V. Ozolins, K. Suenaga, X. Duan, B. Dunn, Y. Yamamto, O. Terasaki, O. M. Yaghi, *Chem. Mater.* **2012**, *24*, 3511–3513; c) T. Kambe, R. Sakamoto, T. Kusamoto, T. Pal, N. Fukui, K. Hoshiko, T. Shimojima, Z. Wang, T. Hirahara, K. Ishizaka, S. Hasegawa, F. Liu, H. Nishihara, *J. Am. Chem. Soc.* **2014**, *136*, 14357–14360; d) J.-H. Dou, L. Sun, Y. Ge, W. Li, C. H. Hendon, J. Li, S. Gul, J. Yano, E. A. Stach, M. Dincă, *J. Am. Chem. Soc.* **2017**, *139*, 13608–13611; e) J. Park, A. C. Hinckley, Z. Huang, D. Feng, A. A. Yakovenko, M. Lee, S. Chen, X. Zou, Z. Bao, *J. Am. Chem. Soc.* **2018**, *140*, 14533–14537.

[11] a) M. Eddaoudi, D. B. Moler, H. Li, B. Chen, T. M. Reineke, M. O'Keeffe, O. M. Yaghi, *Acc. Chem. Res.* **2001**, *34*, 319–330; b) O. M. Yaghi, M. O'Keeffe, N. W. Ockwig, H. K. Chae, M. Eddaoudi, J. Kim, *Nature* **2003**, *423*, 705–714; c) H.-L. Jiang, T. A. Makal, H.-C. Zhou, *Coord. Chem. Rev.* **2013**, *257*, 2232–2249.

[12] a) R. Murase, C. F. Leong, D. M. D'Alessandro, *Inorg. Chem.* **2017**, *56*, 14373–14382; b) M. Souto, K. Strutyński, M. Melle-Franco, J. Rocha, *Chem. Eur. J.* **2020**, *26*, 10912–10935; c) B. Ding, M. B. Solomon, C. F. Leong, D. M. D'Alessandro, *Coord. Chem. Rev.* **2021**, *439*, 213891.

[13] L. Sun, C. H. Hendon, S. S. Park, Y. Tulchinsky, R. Wan, F. Wang, A. Walsh, M. Dincă, *Chem. Sci.* **2017**, *8*, 4450–4457.

[14] a) M. L. Mercuri, F. Congiu, G. Concas, S. A. Sahadevan, *Magnetochemistry* **2017**, *3*, 17; b) L. E. Darago, M. L. Aubrey, C. J. Yu, M. I. Gonzalez, J. R. Long, *J. Am. Chem. Soc.* **2015**, *137*, 15703–15711; c) J. A. DeGayner, I.-R. Jeon, L. Sun, M. Dincă, T. D. Harris, *J. Am. Chem. Soc.* **2017**, *139*, 4175–4184; d) J. A. DeGayner, K. Wang, *J. Am. Chem. Soc.* **2018**, *140*, 6550–6553; e) M. E. Ziebel, L. E. Darago, J. R. Long, *J. Am. Chem. Soc.* **2018**, *140*, 3040–3051; f) S. A. Sahadevan, A. Abhervé, N. Monni, C. Sáenz de Pipaón, J. R. Galán-Mascarós, J. C. Waerenborgh, B. J. C. Vieira, P. Auban-Senzier, S. Pillet, E.-E. Bendeif, P. Alemany, E. Canadell, M. L. Mercuri, N. Avarvari, *J. Am. Chem. Soc.* **2018**, *140*, 12611–12621; g) R. Murase, C. J. Commons, T. A. Hudson, G. N. L. Jameson, C. D. Ling, K. S. Murray, W. Phonsri, R. Robson, Q. Xia, B. F. Abrahams, D. M. D'Alessandro, *Inorg. Chem.* **2020**, *59*, 3619–3630.

[15] a) H. Chen, M. Armand, M. Courty, M. Jiang, C. P. Grey, F. Dolhem, J.-M. Tarascon, P. Poizot, *J. Am. Chem. Soc.* **2009**, *131*, 8984–8988; b) Z. Meng, C. G. Jones, S. Farid, I. U. Khan, H. M. Nelson, K. A. Mirica, *Angew. Chem. Int. Ed.* **2022**, *61*, e202113569; *Angew. Chem.* **2022**, *134*, e202113569.

[16] a) X. Wu, Y. Qiu, Z. Chen, B. Guan, X. Hao, A. I. Rykov, Y. Sun, L. Liu, Y. Zou, J. Sun, W. Xu, D. Zhu, *Angew. Chem. Int. Ed.* **2020**, *59*, 20873–20878; *Angew. Chem.* **2020**, *132*, 21059–21064; b) G. Chen, L. B. Gee, W. Xu, Y. Zhu, J. S. Lezama-Pacheco, Z. Huang, Z. Li, J. T. Babicz, S. Choudhury, T.-H. Chang, E. Reed, E. I. Solomon, Z. Bao, *J. Am. Chem. Soc.* **2020**, *142*, 21243–21248.

[17] a) O. Karagiaridi, W. Bury, E. Tylianakis, A. A. Sarjeant, J. T. Hupp, O. K. Farha, *Chem. Mater.* **2013**, *25*, 3499–3503; b) E. A. Kapustin, S. Lee, A. S. Alshammari, O. M. Yaghi, *ACS Cent. Sci.* **2017**, *3*, 662–667; c) C. Schneider, D. Bodesheim, J. Keupp, R. Schmid, G. Kieslich, *Nat. Commun.* **2019**, *10*, 4921.

[18] a) G. Skorupskii, B. A. Trump, T. W. Kasel, C. M. Brown, C. H. Hendon, M. Dincă, *Nat. Chem.* **2020**, *12*, 131–136; b) J. Y. Choi, J. Flood, M. Stodolka, H. T. B. Pham, J. Park, *ACS Nano* **2022**, *16*, 3145–3151.

[19] a) T. Yamashita, P. Hayes, *Appl. Surf. Sci.* **2008**, *254*, 2441–2449; b) J. Conradie, E. Erasmus, *Polyhedron* **2016**, *119*, 142–150.

[20] R. M. Buchanan, S. L. Kessel, H. H. Downs, C. G. Pierpont, D. N. Hendrickson, *J. Am. Chem. Soc.* **1978**, *100*, 7894–7900.

[21] P. Gütlich, A. B. Gaspar, Y. Garcia, *Beilstein J. Org. Chem.* **2013**, *9*, 342–391.

[22] N. Shaikh, S. Goswami, A. Panja, X.-Y. Wang, S. Gao, R. J. Butcher, P. Banerjee, *Inorg. Chem.* **2004**, *43*, 5908–5918.

[23] a) A. Dei, D. Gatteschi, L. Pardi, U. Russo, *Inorg. Chem.* **1991**, *30*, 2589–2594; b) K. A. Collins, R. J. Saballos, M. S. Fataftah, D. Puggioni, J. M. Rondinelli, D. E. Freedman, *Chem. Sci.* **2020**, *11*, 5922–5928.

[24] A. Leonarska, M. Kądziołka-Gaweł, A. Z. Szeremeta, R. Bujakiewicz-Korońska, A. Kalvane, A. Molak, *J. Mater. Sci.* **2017**, *52*, 2222–2231.

[25] J. P. Perdew, K. Burke, M. Ernzerhof, *Phys. Rev. Lett.* **1996**, *77*, 3865–3868.

[26] S. Grimme, J. Antony, S. Ehrlich, H. Krieg, *J. Chem. Phys.* **2010**, *132*, 154104.

[27] a) G. Kresse, J. Hafner, *Phys. Rev. B* **1993**, *48*, 13115–13118; b) G. Kresse, J. Hafner, *J. Phys. Condens. Matter* **1994**, *6*, 8245–8257; c) G. Kresse, J. Furthmüller, *Comput. Mater. Sci.* **1996**, *6*, 15–50.

[28] I. Choudhuri, D. G. Truhlar, *J. Phys. Chem. C* **2019**, *123*, 17416–17424.

[29] H. J. Kulik, M. Cococcioni, D. A. Scherlis, N. Marzari, *Phys. Rev. Lett.* **2006**, *97*, 103001.

[30] a) M. L. Aubrey, B. M. Wiers, S. C. Andrews, T. Sakurai, S. E. Reyes-Lillo, S. M. Hamed, C.-J. Yu, L. E. Darago, J. A. Mason, J.-O. Baeg, F. Grandjean, G. J. Long, S. Seki, J. B. Neaton, P. Yang, J. R. Long, *Nat. Mater.* **2018**, *17*, 625–632; b) M. Cococcioni, S. de Gironcoli, *Phys. Rev. B* **2005**, *71*, 035105; c) A. Jain, G. Hautier, S. P. Ong, C. J. Moore, C. C. Fischer, K. A. Persson, G. Ceder, *Phys. Rev. B* **2011**, *84*, 045115.

[31] M. Inui, S. A. Trugman, E. Abrahams, *Phys. Rev. B* **1994**, *49*, 3190–3196.

[32] X. Yong, W. Shi, G. Wu, S. S. Goh, S. Bai, J.-W. Xu, J.-S. Wang, S.-W. Yang, *J. Mater. Chem. A* **2018**, *6*, 19757–19766.

[33] a) J. S. Miller, *Chem. Soc. Rev.* **2011**, *40*, 3266–3296; b) J. G. Park, B. A. Collins, L. E. Darago, T. Runčevski, M. E. Ziebel, M. L. Aubrey, H. Z. H. Jiang, E. Velasquez, M. A. Green, J. D. Goodpaster, J. R. Long, *Nat. Chem.* **2021**, *13*, 594–598.

[34] M. Balanda, *Acta Phys. Pol. A* **2013**, *124*, 964–976.

[35] a) S. Chillal, M. Thede, F. J. Litterst, S. Gvasaliya, T. Shaplygina, S. Lushnikov, A. Zheludev, *Phys. Rev. B* **2013**, *87*, 220403; b) J. M. Rojo, J. L. Mesa, L. Lezama, J. L. Pizarro, M. I. Arriortua, J. R. Fernandez, G. E. Barberis, T. Rojo, *Phys. Rev. B* **2002**, *66*, 094406.